



Understanding Zn Electrodeposits Morphology in Secondary Batteries Using Phase-Field Model

Vitaliy Yurkiv, ² Tara Foroozan, Ajaykrishna Ramasubramanian, Marco Ragone, Reza Shahbazian-Yassar, and Farzad Mashayek*

Department of Mechanical and Industrial Engineering, University of Illinois at Chicago, Chicago, Illinois 60607, United States of America

Zinc (Zn) aqueous rechargeable batteries (ZBs) have shown a tremendous success in various applications due to their environmental friendliness, multi-electron capacity, high abundance, safety and low cost; however, analogous to their Li-ion battery counterparts, they suffer from the dendrite formation leading to decrease in capacity and eventual failure. Despite many studies reporting a good performance and partial dendrites suppression, there have been little theoretical systematic studies of Zn electrodeposits morphology analysis in ZBs. In the current work, we present the results from phase-field modeling (PFM) of Zn electrodeposition at different current densities. Different Zn morphologies, such as boulders, mossy and dendritic shape are modeled. The computational model predicts two-dimensional distribution of Zn electrodeposits, Zn²⁺ ions concentration, electrostatic potential, stress and equivalent plastic strain. It was found that the stress has a major influence on the electrodeposition, and vice versa the Zn electrodeposits growth is found to affect the stress distribution significantly. The plastic yielding occurs preferentially at the node of the boulders and through the filaments and mossy structures. The results also provide a basis for development and design of novel strategies against unwanted Zn dendrites formation.

© 2020 The Electrochemical Society ("ECS"). Published on behalf of ECS by IOP Publishing Limited. [DOI: 10.1149/1945-7111/ab7e91]

Manuscript submitted November 30, 2019; revised manuscript received January 31, 2020. Published March 19, 2020.

Supplementary material for this article is available online

One of the fundamental requirements of energy storage technology is the safe and long-lasting operation. With climate change as one of the most prevalent concerns nowadays, finding efficient energy storage technologies is the focus of academic and industrial research. One such technology is metal-based batteries, which have several advantages comparing to their Li-ion counterparts. In particular, zinc (Zn) aqueous batteries (ZBs) using Zn as a negative electrode have a high theoretical capacity (820 mA·h·g⁻¹), compatible with water, beneficially alloying with Li, environmentally benign, high abundance and low cost. However, most, if not all, metal batteries suffer from metal dendrites formation during a longterm operation.³⁻⁵ The formation of Zn dendrites in ZBs causes detrimental effects such as internal short circuit, amplified surfaceoriginated side reactions and mechanical deformation of cell parts up to the breakdown of the battery. Thus, it is critical to understand the mechanism of Zn dendrites formation and growth in ZBs and propose protective strategies to ensure stable, safe and long-lasting operation.

There is a significant foregoing research on ZBs to suppress harmful Zn dendritic electrodeposits. ⁶⁻⁸ Parker et al. ⁹ have suggested to use 3D Zn sponge for dendrite-free cycling, whereas Stock et al. ¹⁰ have proposed anion-exchange ionomer-coated Zn sponge in zinc-oxygen battery to enhance cycling stability. Similar approach has been adopted by Yan et al. ¹¹ to use Zn/Cu foam electrode for zinc-based alkaline batteries. On the other hand, a number of works have been reported using protective coatings, such as bismuth-based oxides ^{12,13} and reduced graphene (rGO) oxide. ¹⁴ In particular, rGO has also been used as a mechanical barrier to suppress Zn dendrites. ¹⁵ Also, there are few reports using different kinds of additives for Zn dendrite suppression. However, all these prior studies are based upon the trial-and-error approach, since the analysis of Zn electrodeposit morphologies is challenging in real battery applications.

On the other hand, modeling techniques, ^{16–19} allow the investigation of Zn dendrites formation and growth under different conditions for better understanding and analysis of their morphologies and correspondingly the suppression mechanisms. The most promising and effective method is the phase-field modeling (PFM),

which has been applied to many electrochemical deposition problems. ^{19–23} The pioneered and outstanding quantitative phasefield modeling of Zn electrodeposition was performed by Cogswell.²⁰ In this PFM work, the Marcus kinetics for concentrated solutions using grand electrochemical potential and electroneutrality is formulated to eliminate the Debye length. The results of his PFM agree well with zinc Faradaic reaction kinetics, tip velocity, fractal growth dimensions and radius of curvature. It is known that due to the high Young's modulus of Zn, the mechanical deformation of electrodeposited morphologies could have a significant influence on the formation and the growth of Zn dendrites.²⁴ As a result, in the present work we have extended our prior PFM calculations by including the mechanical properties of Zn to evaluate the influence of elastic energy density on electrodeposition process. In addition, we have performed a detailed analysis of electrodeposited Zn morphologies at different current densities, allowing for more profound understanding of their formation and growth. This in turn could help in the development of new strategies to prevent dendritic growth.

Many studies have used term "dendrite" to denote Zn electrodeposits in ZBs. It is briefly described in our previous work²¹ as well as in other works^{25,26} on the topic of metal-based batteries, that the term "dendrite" (from Greek dendron— $\delta \acute{\epsilon} \nu \delta \rho o \nu$ —meaning "tree") should be used to describe the classical branched fractal structure. Such structure is formed in the case of high current density of Zn²⁺ electrodeposition²⁷ only; however, mossy zinc deposition condition is unusual as they form at low current densities. In the case of Zn dendrites depositing at high current densities, the growth can be explained by concentration change of ions near electrode surface. However, such a simplified diffusion limited model cannot be applied to the mossy structure evolution since a diffusion limited model is not applicable under low current density scenarios. We should also note that, in Li-metal batteries, electrodeposition in the form of real fractal branched structure was not observed, instead filaments, whiskers and mossy structures were reported.²⁶

Also, we would like to clarify the usage of the term "solid electrolyte interface"—SEI—in application to the ZBs before describing the details of modeling methodology in this work. As it is known, the SEI is the key component of "traditional" electrolyte-based energy storage technologies such as Li-ion batteries (LIBs), ²⁹ it stabilizes electrolytes (e.g., LiPF₆, EC/DMC) at electric potentials beyond their thermodynamic stability limits, allowing

^{*}Electrochemical Society Member.

^zE-mail: vyurkiv@uic.edu

electrochemical reactions proceed reversibly. Until recently, it was believed that the SEI can only be formed in non-aqueous media; however, recent studies have shown that the SEI concept can be applied also to aqueous electrolytes, explaining many experimentally observed phenomena. Only In LIB, SEI is formed as a result of irreversible decomposition of electrolyte at the surface of electrodes. This concept is also applied to aqueous LIB; however, in ZBs the surface layer at the interface between the Zn electrode and electrolyte forms as a result of solid Zn oxidation forming primarily ZnO layer. Although the functionality of this ZnO layer on top of the Zn electrode is very similar to the SEI in LIB, it does not entirely form from the decomposition of the electrolyte as in the traditional SEI. However, in this work we call this ZnO surface layer the SEI analogous to the prior studies on LIBs SEI.

In this work, we present the results from the PFM calculations of Zn electrodeposition in Zn aqueous battery. Although, we consider Zn aqueous battery as a practical application, our simulation results do not cover all types of ZB. Specifically, different electrodeposits (especially in the SEI layer) may form depending on the pH of an electrolyte. The primary objective of this work is to explore the influence of current density on electrodeposit morphologies for electrolyte close to the neutral pH. This study largely uses our previously developed PFM of metal electrodeposition adapted to the specifics of Zn battery. In addition, we have performed scanning electron microscopy (SEM) measurements of Zn electrodeposition to support our PFM calculation.

Methodology

Experimental.—Zn electrodeposition: All the electrodeposition experiments were carried out in a quartz cell using Cu as positive electrode and Zn metal foil as negative electrode. Mild 2 M ZnSO₄·H₂O with PH \sim 6 was used as electrolyte. Different current densities of 2, 10 and 15 mA·cm⁻² were applied to electrodeposit Zn onto the Cu substrate. Capacity was kept at 3 mAh·cm⁻² for all the depositions. Bio-Logic VMP3 Electrochemical Workstation equipped with EC-Lab software was used for controlling the electrodeposition process.

Scanning electron microscope (SEM) Imaging: Reith e-LiNE 100 Electron Beam Lithography System was used for SEM imaging. SEM experiments were performed with an acceleration voltage of 10 kV and a working distance of 10 mm.

Modeling overview.—In our previous work, 21 we have developed the PFM of metal electrodeposition and applied it to study Li precipitation in Li-metal battery. 19,21 The model follows fundamental thermodynamic and electrochemical concepts of electrodeposition and is thoroughly described in our previous work as well as other related works, $^{22,32-34}$ thus, only a brief summary is given here. The model is developed in the MOOSE framework and is formulated in continuum theory based upon diffusion-conservation laws using partial-differential equations and then discretized using finite element method 35 and solved computationally. For the present calculations, a 2D square computational domain (5 × 5 μ m 2) is used for all cases (Fig. 1, lower panel).

The modeling domain is composed of two phases, namely the liquid electrolyte phase and the Zn solid phase. Different processes such as ions diffusion and electro-migration in the liquid phase, electrical conductivity and elasto-plastic deformation in the solid phase, anisotropic solid-state growth and charge-transfer reaction at the interface between the solid and liquid phases, are taken into consideration in the present PFM calculations. In the framework of the PFM, the evolution of all these processes is described by the following total free energy functional $(F(\xi, c_i, \varphi, u))^{21}$

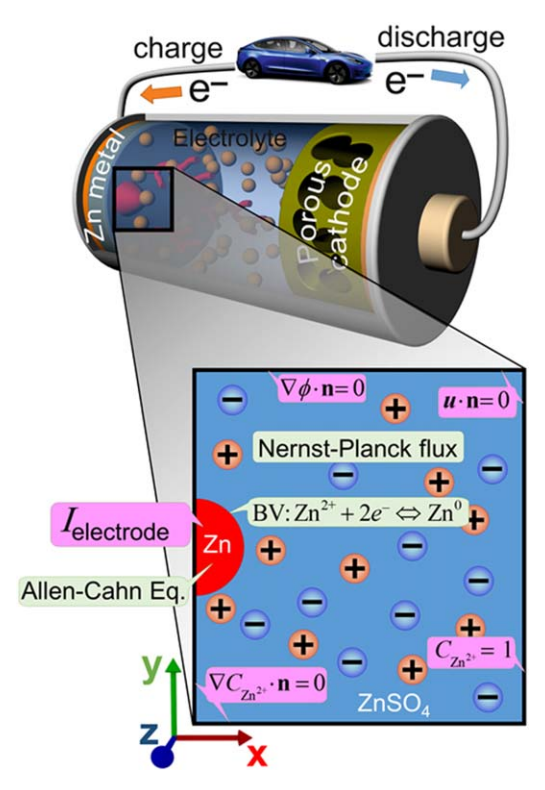


Figure 1. Illustration of Zn battery configuration highlighting dendrites formation on the Zn metal electrode (upper picture) and details of the phase-field model (lower picture). In the lower picture magenta colored boxes depict boundary conditions and light-green boxes describe the physics of different processes modeling. Definitions of symbols and terms are given in the text. Structural details are not to scale and are merely for illustration purposes.

$$F(\xi, c_{i}, \varphi, u) = \int_{V} \left[f_{ch}(\xi, c_{i}) + \frac{1}{2} \kappa_{\xi} (\nabla \xi)^{2} + f_{elch}(\xi, c_{i}, \varphi) + f_{els}(u, \xi) + f_{pl}(u) + f_{ns}(c_{i}) \right] dV,$$
[1]

where, $f_{ch}(\xi, c_i)$ is the chemical free energy density represented by the double-well function; $\kappa_{\xi}(\nabla \xi)^2$ accounts for excess of the free energy at the interface between the solid and liquid phases, with κ_{ξ} being the gradient energy coefficient; $f_{elch}(\xi, c_i, \varphi)$ is the electrochemical free energy density; $f_{els}(u, \xi)$ describes the elastic free energy density; $f_{pl}(u)$ is the plastic free energy density; $f_{ns}(c_i)$ is the energy density that accounts for random ions diffusion through the SEI $(f_{ns}(c_i) = h'(\xi)\chi\psi$, with $h'(\xi)$ being the first derivative of tilting function with respect to the non-conserved order parameter, χ is a random number and ψ is an amplitude of fluctuation). The detailed reaction-diffusion mechanism of Zn through the SEI provides a more comprehensive description of Zn random delivery to the Zn/SEI interface than the usage of random noise approach described above. However, it is impractical for the full PFM model to consider the entire length- and time-scale spectra to incorporate microstructural details of the SEI at the nanometer scale. Thus, in the present work, we have employed an averaging approach, which foresees an approximate representation of the SEI within a representative narrow volume at the electrode/electrolyte interface that is relatively small comparing to overall dimensions; however, it has a significant effect due to its nature. The gradient energy coefficient (κ_{ε}) is modeled by taking into account the surface energy anisotropy³⁶ as $\kappa_{\xi} = \kappa_{\xi}^{0}[1 + \delta \cos{(\omega \theta)}]$, with κ_{ξ}^{0} is the surface energy; δ is the strength of the anisotropy; ω is the mode of the anisotropy and θ is

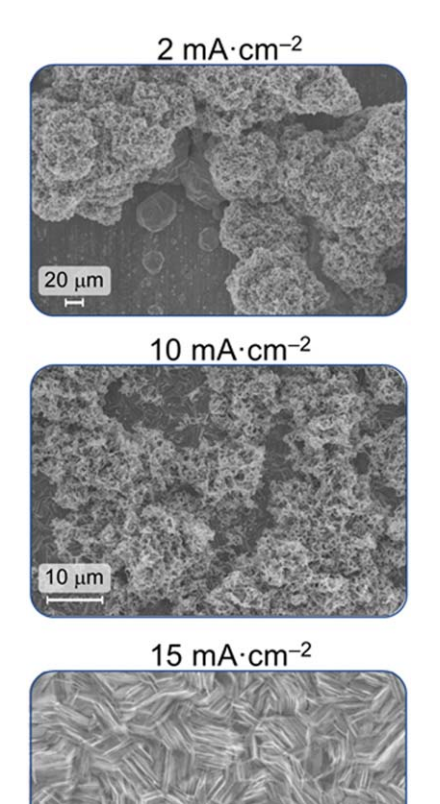


Figure 2. Scanning electron microscopy images of Zn electrodeposits at 2, 10 and 15 mA cm⁻².

Table I. Model parameters used in the simulations.

Parameter	Value	References
General		
Modeling domain size	$5 \times 5 \mu \text{m}^2$	Set
Temperature	298 K	Set
Zn related		
c_{11}	163 GPa	43
c_{12}	31 GPa	43
c_{13}	48 GPa	43
c_{33}	60 GPa	43
c_{44}	39 GPa	43
Yield strength	27 MPa	43
Molar volume, $V_{\rm m}$	$9.16 \cdot 10^{-6} \text{ m}^3 \cdot \text{mol}^{-1}$	Calculated
Surface energy (κ_{ξ}^0)	$0.5 \text{ J} \cdot \text{m}^{-2}$	29
Electrical conductivity	$1.69 \cdot 10^7 \text{ s} \cdot \text{m}^{-1}$	45
Electrolyte		
Zn ²⁺ diffusion coefficient	$3.68 \cdot 10^{-10} \text{ m}^2 \cdot \text{s}^{-1}$	44
Electrical conductivity	$0.1 \text{ s} \cdot \text{m}^{-1}$	45

the angle between the surface normal and the crystallographic orientation.

The Butler-Volmer equation is used to describe charge-transfer reaction at the solid/liquid interface. The transport of electrons in the solid Zn phase and ions in the electrolyte phase is modeled using the Nernst-Planck-Poisson's model, in which the ion flux is governed by a Nernst-Planck relation and the electrostatic potential is established

to enforce electroneutrality. In addition, perfect conductivity of Zn solid phase is assumed.

The elastic-plastic model accounts for the solid phase mechanical deformation during Zn electrodeposition using the elastic stiffness and strain tensors. The plastic energy density is concentration independent,³⁷ where the associated J_2 -flow rule for the plastic stretch is used.³⁸ In addition, the power-law hardening rule with von Mises stress criterion to determine the point of plastic yielding is used.

Computational implementation.—The coupled system of partial differential equations describing processes overviewed above is solved using the MOOSE framework. 35,39 The numerical solution is obtained by solving iteratively and sequentially the solid-state growth, the electric potential distribution, the liquid species transport, the electrochemical reaction and the mechanical modules. The adaptive mesh refinement 40 is used. Since the charge-transfer reaction occurs at the ultra-thin layer between the solid and liquid phases, and due to the nature of diffusive interface-based PFM, at least three elements per interface are ensured. Such a fine mesh is not needed outside the interface; thus, a coarse mesh is used elsewhere. Following general experimental principles, we set the concentration of Zn-ions to one and the current flow into the solid Zn is constrained by an integral over the active area at the electrode.⁴¹ At the other boundaries, zero-gradient boundary conditions are used. Two-dimensional plain-strain assumption is invoked, meaning that out of plain strain vanishes ($\varepsilon_{zz} = 0$). More details about the present PFM, definition of the symbols and the computational implementation are given in Ref. 21.

Results and Discussion

Considering the fact that mossy deposition of Zn at low current density does not follow a simplified diffusion limited model applicable to the case of other metals such as Li, the main aim of this work is to understand Zn electrodeposition mechanism at different current densities. For an in-depth understanding of the Zn electrodeposition processes, we study the formation and evolution of Zn hexagons, mossy and dendritic structures. It is generally difficult to measure experimentally the evolution of such Zn electrodeposits over time in real cells, thus there is a lack of in-depth experimental analysis of Zn electrodeposition morphologies for different current densities. On the other hand, simulations of random structures following experimentally observed tendencies are usually employed. Below we present such an analysis at different current densities employing parameters described in the following section. In addition, we use our own experimental SEM measurements to reveal Zn electrodeposit morphologies.

SEM measurements of Zn electrodeposit morphologies.—Figure 2 presents the experimental SEM measurements of different Zn morphologies obtained at 2, 10 and 15 mA·cm⁻². At both current densities of 2 mA·cm⁻² and 10 mA.cm⁻², boulder-type Zn forms, which transforms to bush-like structures at later stages. However, we should note that the transition between boulders and filaments happen at earlier stages of growth when applying lower current densities. This observation is consistent with literature, ^{3,42} and happens as a result of more local current density variations at lower applied currents. If a sufficient current density is applied (15 mA·cm⁻²) dense hexagons, mainly parallel to the electric field and under diffusion-controlled reaction, are formed. Based upon our measurements we have used these experimental conditions in the PFM calculations described below.

Material properties.—All material properties are summarized in Table I. The modeling domain is set to be $5 \times 5 \ \mu\text{m}^2$, where the solid dendritic phase grows from the left boundary and the right boundary is set to be the electrolyte. The solid phase is pure Zn metal with electric conductivity of $1.69 \cdot 10^7 \, \text{s·m}^{-1}$ and a surface

energy of $0.5 \,\mathrm{J\cdot m^{-2}}$. The elasticity model accounts for the elastic deformation of the Zn solid phase. Owing to the hexagonal structure of Zn, there are five independent elastic constants, i.e., c_{11} , c_{12} , c_{13} , c_{33} , c_{44} (see Table I for values). The yield strength of Zn is 27 MPa. The electrolyte consists of binary ZnSO₄·H₂O solution (water is a solvent), where the Zn²⁺ diffusion coefficient is set to $3.68\cdot10^{-10}\,\mathrm{m^2\cdot s^{-1}}$, and the electrical conductivity of the liquid is $0.1\,\mathrm{s\cdot m^{-1}}$. The Zn²⁺ concentration is normalized by the maximum concentration in the electrolyte ($c_{2n}^{\mathrm{max}} = 1 \times 10^3\,\mathrm{mol\cdot m^{-3}}$) and the solid Zn concentration (e.g., molar site density) is normalized by $c_{2n}^{\mathrm{max}} = 1.09 \times 10^5\,\mathrm{mol\cdot m^{-3}}$. We assume that the surface energy (κ_{ξ}^0) is constant with a value of $0.5\,\mathrm{J\cdot m^{-2}}^{-2.9}$ According to Zn hexagonal crystal structure, the mode of the anisotropy is set to $\omega=6$. The rate of electrochemical reaction (k) is adjusted to meet the electrodeposition rate and it is equal to $2\times 10^{-8}\,\mathrm{m^{2.5}\cdot mol^{-0.5}\cdot s^{-1}}$, which is consistent with the prior measurements.

Low density.—Many experimental prior observations^{3,4,42,46} suggest that the Zn electrodeposition starts with the formation of hexagonal boulders, which further growth into different shapes, such as mossy, layered, boulders and dendrites moving from low to high current densities, respectively. We begin our analysis with a simple case of two nuclei, where the electrodeposition occurs. Figure 3 shows transient solution profiles for the nominal problem of Zn electrodeposition at a low current density of 2 mA·cm⁻². Two hexagon-shape boulders evenly grow from the left towards the bulk electrolyte. Such an initial geometry is chosen to mimic the surface of the current collector in the real battery, which is uneven with random nano-elevations and nano-valleys. These nanoelevations create a local enhancement of electric potential, where the Zn dendrites could form. 3,4,42,46 Since the surface roughness is uncontrollable, it is reasonable to assume two random nuclei with arbitrary separation. As an example of random formation of Zn boulders, we have performed the Zn electrodeposition experimental measurements at a current density of 2 mA·cm⁻², which is shown in the inset picture in Fig. 3 on the right. A few submicron hexagonal boulders are clearly visible in this picture, as well as the formation of mossy structures, which appear at the later stages of the growth. Similarly, as in these experiments, we have performed PFM simulations, where first two hexagon-like boulders are formed with transition to filaments shapes. Once the mossy structure initiates, it preferentially evolves. Continuous increase in surface area boosts variation of local current density in the adjacent areas further suppressing the deposition of boulders. The Zn filaments could be formed as a result of random diffusion of Zn-ions through the anisotropic SEI, towards the solid Zn phase. Due to the complicated structure and small thickness of the SEI, it is very challenging to identify and characterize the exact SEI structure and its properties, experimentally. Moreover, the properties of the SEI grain boundary depend upon the applied potential and the properties of the electrolyte.⁴⁷ The attempt to take into account all these morphological details of the SEI for the modeling of the Zn electrodeposition at large scale, is essentially impossible. There have been some reports on the SEI influence of electrodeposition in ZBs. 3,4,46 This includes a study on Zn diffusion mechanism through the thin $(\sim 20 \text{ nm})$ ZnO layer formed on top of the Zn electrode. Such a detailed diffusion mechanism captures the entire range of the processes occurring in the ZnO SEI layer, whereas the present approach based on the energy density noise in the energy functional cannot. However, developing a detailed diffusion-reaction mechanism requires a great deal of multi-disciplinary efforts. In particular, cryo-spectroscopic techniques such as transmission electron microscopy (TEM), electrochemical measurements in lab-scale experiments combined with ab-initio calculations (e.g., density functional theory—DFT) can help to understand fundamentals of Zn diffusion through ZnO layer. Nevertheless, even having such a mechanism would be a challenge to relate the real microstructural features observed within the ZnO nanofilm with PFM simulations needs, thus some assumptions must be made. As described above,

such an assumption in our present work is the random noise field at the interface between the solid and liquid phases. This approach leads to formation of different filaments with sizes between 200 to 300 nm as can be observed in third and fourth columns in Fig. 3.

We next analyze the mechanical response during the formation of boulders and filaments. These results are shown in Fig. 3 (last three rows) in the form of the normal stress components in x and y directions and the equivalent plastic strain. A significant compressive stress develops at the interface of the boulders and the liquid phase, causing the formation of filaments/mossy structures. Such a significant interfacial stress builds up as a result of electrodeposition, random Zn delivery and the mechanical properties of Zn. Further analysis of the mechanical behavior of boulders and filaments shows that the significant plastic yielding (fifth row) occurs in the later stages of the growth preferentially in the narrow filaments and at the nodes of the boulders. We have also performed some additional PFM calculations of Zn electrodeposition at the same current density (2 mA·cm⁻²), however assuming a pre-deposited thin Zn layer as initial conditions (Fig. S1 is available online at stacks.iop.org/JES/ 167/060503/mmedia). All parameters and conditions are kept the same as in the case presented above, the only difference is the initial condition (i.e., two nuclei against a thin film). As can be seen in Fig. S1 there is no significant difference in final Zn morphology and mechanical response of electrodeposits comparing to Fig. 3 despite very different initial conditions. The only noticeable difference is the initial growth stage, specifically in the case of two nuclei we observe the formation of hexagon-like structures, whereas for the thin film, the electrodeposition starts as a film with the transition to filaments.

The formation of such filaments could have harmful effects on the cell, since these narrow electrodeposits could easily penetrate through the separator leading to the internal short circuit. Correspondingly, experimental efforts should be concentrated on the reduction of such filament formation by, for example, increasing the mobility of Zn^{2+} ions in the electrolyte or decreasing the internal stress build-up in the hexagonal boulders at the earlier stages of the growth. In addition, experimental efforts could be also devoted to enhance Zn^{2+} diffusion through the ZnO surface nanolayer, in order to prevent random electrodeposition.

Intermediate current density.—This section presents the results of the PFM simulation at intermediate current density. Specifically, two cases are served to demonstrate capabilities of the model i.e., 10 mA·cm⁻² and 15 mA·cm⁻². These two values of the current density are chosen since in this range the transition from random boulders and filaments formation to the well-organized compact hexagons electrodeposits occurs. Figure 4 shows the results for the first case of 10 mA·cm⁻², for which five nuclei, as an initial condition, are assumed to be present. Similarly, as in the previous 2 mA·cm⁻² case, equally sized hexagons are formed at the beginning, which start to mechanically interact after approximately 2 min causing a significant compressive stress build-up between the hexagons. The synergistic effects of the stress increase and the random Zn²⁺ diffusion through the ZnO nanolayer cause the formation of bush-like structures on the top of the hexagons. Comparing the results presented in Figs. 3 and 4, it could be observed that for the 10 mA·cm⁻² case a higher Zn²⁺ concentration gradient is developed for the filaments with almost equal stress values for both cases. Based upon the results presented in Figs. 3 and 4, we can also conclude that the transformation from the boulders to bush-like structures does not cause a significant stress difference. Thus, most probably the branching of the boulders is triggered by the presence of defects at the anode surface (e.g., defective SEI morphology). Comparing the equivalent plastic strain for both cases, similar situation is observed, where yielding occurs primarily through the filaments and at the nodes. In addition, some yielding appears at the root, due to the mechanical interaction of the boulders.

The increase of the current density from $10 \,\mathrm{mA \cdot cm^{-2}}$ to $15 \,\mathrm{mA \cdot cm^{-2}}$ causes the formation of compact hexagons without the formation of filaments and bush-like structures at the beginning.

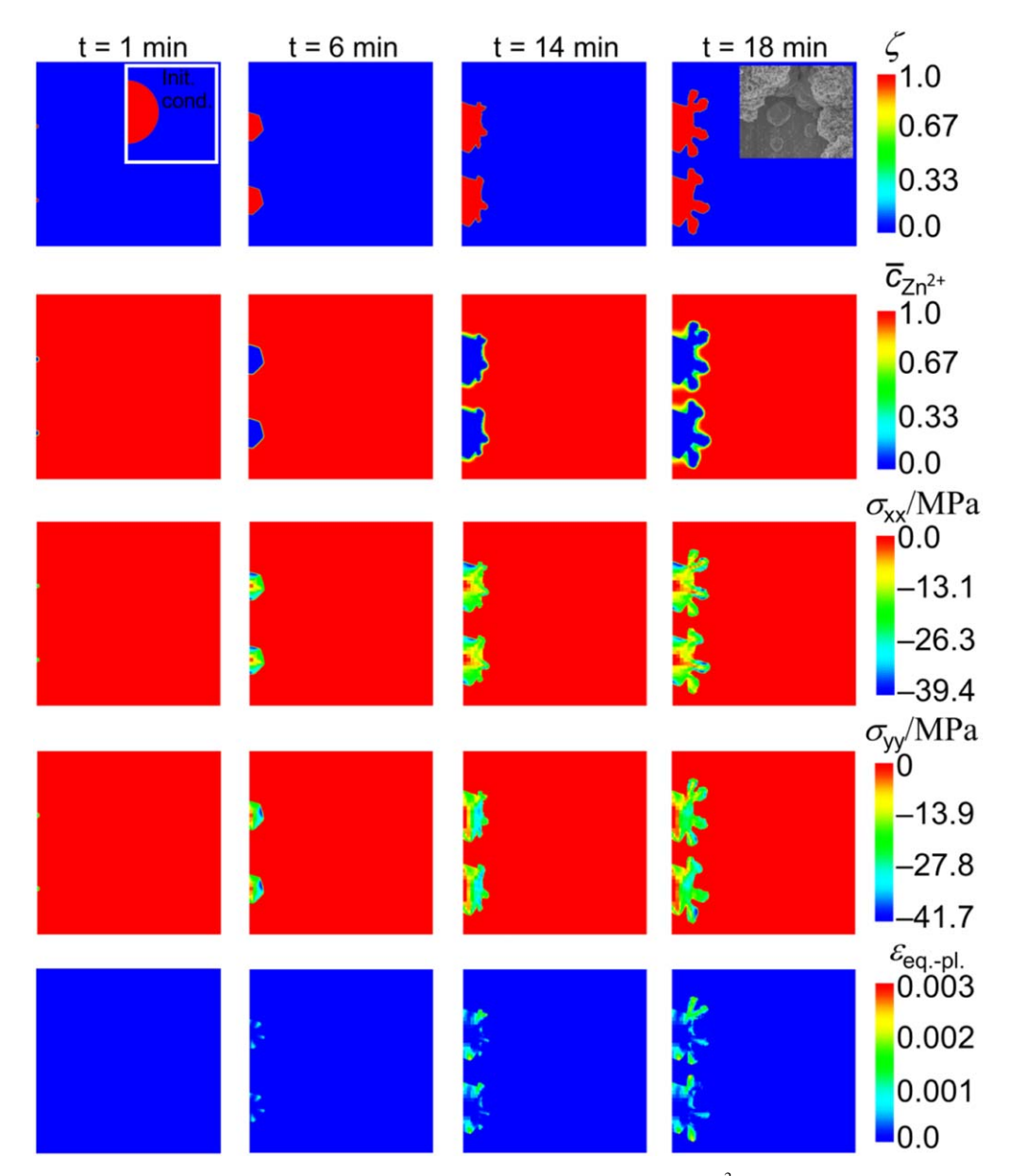


Figure 3. The PFM simulation results of the Zn electrodeposition at the current density of 2 mA·cm⁻². First row shows solid Zn boulders and filaments formation; second row depicts the change of Zn²⁺ concentration in the electrolyte; the third and fourth rows show the normal stress components (σ_{xx} and σ_{yy}); the fifth row illustrates the equivalent plastic strain.

We have modeled two cases: the merging and non-merging electrodeposits, since both cases are observed in the experiments, as it is shown in the inset in Fig. 5 in the last picture of the first row. It is very challenging to study these cases experimentally due to the complicated structures and the transient nature of Zn electrodepositions, however, from the modeling standpoint these cases could be separated into individual calculations. Correspondingly, it enables a more profound understanding of the origin of such electrodeposit morphologies. The physical origin of the merging and non-merging boulders lays in the mechano-chemical properties of the SEI. Specifically, for thicker ZnO layer, forming in alkaline electrolytebased batteries, it is expected to see non-merging boulders, whereas for a thin surface layer, the top SEI layer is not fully developed, thus it could break and lead to the merging of the boulders. Due to the limited knowledge about the SEI's mechano-chemical properties at the nanoscale it is not possible to take these details into account, specifically at the scale of the PFM calculations. Thus, in the present work merging boulders case is realized by lowering the surface energy coefficient $(\kappa_{\varepsilon}^{0})$ by a factor of two in the calculation of the

free energy at the interface between the solid and liquid phases. In general, lowering the surface energy coefficient to mimic the SEI nanoscale properties is a reasonable strategy for the modeling approach; however, it is definitely not assured for a specific electrolyte and the specific SEI composition. Nevertheless, this approach allows to study complicated Zn electrodeposition processes at micro- and seconds scales. Figure 5 presents the results of Zn electrodeposition at 15 mA·cm⁻² setting three identical nuclei as the initial condition. The same as in the previous cases illustrated above, equal hexagons are formed at the beginning; however, at the later stages the mechanical deformation causes the outside boulders to grow bigger comparing to the middle one. The further increase of the stress causes the deformation of the boulders, resulting in elongated parts at the top, which may lead to filaments formation at the later stages of the growth. It should be noted that in this case of three boulders, the highest stress is observed at the root between the boulders, causing a significant plastic strain as it is shown in the last row of Fig. 5.

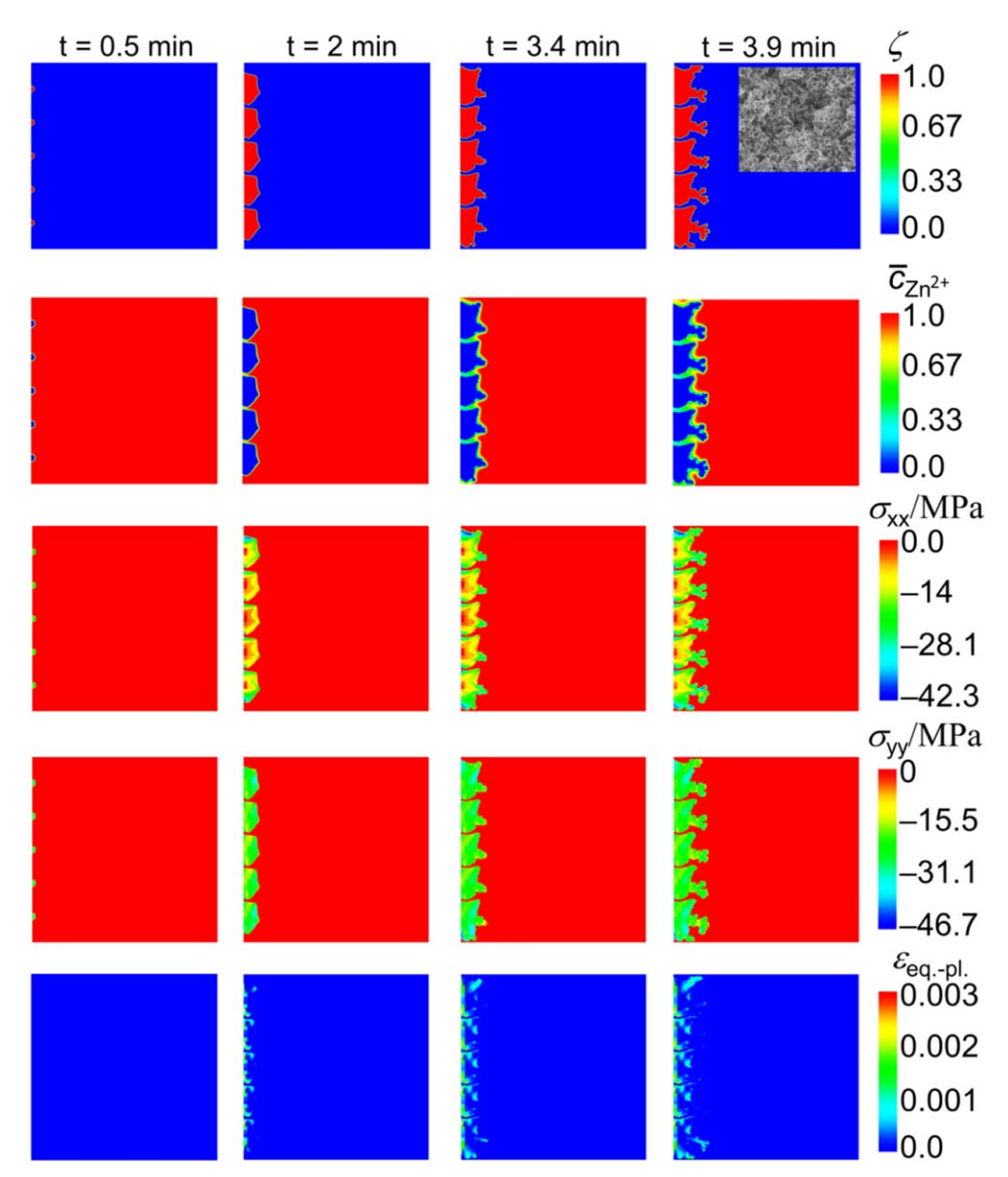


Figure 4. The PFM simulation results of the Zn electrodeposition at the current density of 10 mA·cm⁻². First row illustrates solid Zn boulders and filaments formation; second row depicts the change of Zn^{2+} concentration in the electrolyte; the third and fourth rows show the normal stress components (σ_{xx} and σ_{yy}); the fifths row demonstrates the equivalent plastic strain.

Figure 6 represents a similar electrodeposition progression to the previous case shown in Fig. 5, however for the case of merging hexagons. In Fig. 6, the same as in Fig. 5, the growth starts at a uniform rate for each nucleus; however, at the later stages they merge creating one solid piece. As illustrated, the merging begins at the bottom and it progresses to the top with a general trend similar to the case of non-merging electrodeposits. However, due to the small stress, the deformation of the neighboring nucleus is smaller. Such mechanical relaxation is not observed in the case of non-merging particles. As a consequence, the equivalent plastic strain develops non-uniformly, with a similar general trend as in the results presented above.

High current density.—Finally, we consider the case of a very high current density of 100 mA·cm⁻². In these conditions, the true dendritic structures are observed, where "leaves" for each hexagon boulder node are formed. These morphological features agree well with the prior experimental measurements, 3 where the morphology is under single-factor control of diffusion. Figure 7 illustrates the

electrodeposition at current density of 100 mA·cm⁻², where the Zn solid phase growth (first row), the change of the Zn²⁺ concentration (second row), the different normal components of the Cauchy stress tensor (third and fourth row) and the equivalent plastic strain (fifth row) are shown. The concentration evolution near the dendritic electrodeposits follows a similar trend as in the above results. However, the components of the Cauchy stress tensor show slightly different situation, specifically, through the center of each "leaf" a uniform stress develops, whereas the highest stress forms at some interfaces only. This causes a significant equivalent plastic strain in the center comparing to the interfaces between the solid and the liquid phases.

At this point we would like to compare the Li and Zn electrodeposition processes. In our previous work, ²¹ we have performed the PFM calculations of various scenarios of Li electrodeposition including filaments formation, dense bushes growth as well as their transitions. Due to the nature of Li metal and the evolution of electrodeposits, ⁴⁸ much lower stress development was observed comparing to the Zn electrodeposition. This is due to a

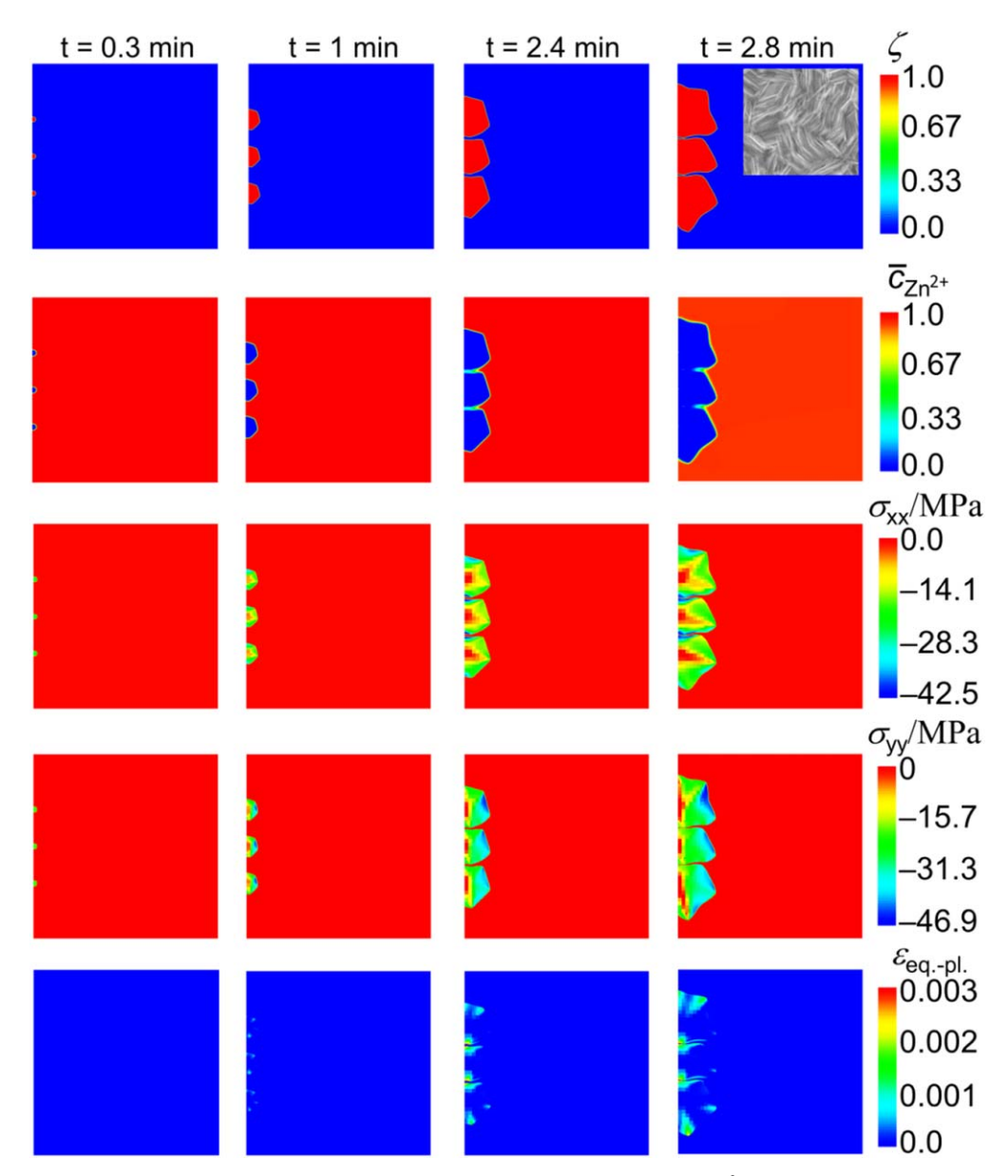


Figure 5. The PFM simulation results of the Zn electrodeposition at the current density of 15 mA·cm⁻². First row shows solid Zn boulders and filaments formation; second row depicts the change of Zn²⁺ concentration in the electrolyte; the third and fourth rows show the normal stress components (σ_{xx} and σ_{yy}); the fifths row demonstrates the equivalent plastic strain.

significant difference between mechanical properties of Li comparing to Zn (the Young's modulus of Zn is almost an order of magnitude bigger than that of Li). This in principle could help to explain the influence of stress on electrochemistry. In particular, in the case of Zn electrodeposition, higher compressive stresses will significantly change electrochemical charge-transfer rate comparing to the lower stress values in the Li electrodeposition.

Following the results presented in this work, a few quantitative suggestions could be made. In the prior literature, ^{49,50} the inclusion of stress in electrochemical kinetics usually follows the modified Butler-Volmer equation⁵⁰

$$i = i_0 \exp\left[\frac{(\beta_{\rm m} - \beta)\Omega\sigma_{h,\rm surf}}{RT}\right] \left[\exp\left(\frac{(1-\beta)F\eta}{RT}\right) - \exp\left(\frac{\beta F\eta}{RT}\right)\right],$$
 [2]

where, i_0 is the exchange current density; $\beta_{\rm m}$ is the mechanical symmetry factor; β is the symmetry factor; Ω is the partial molar volume; $\sigma_{h,surf}$ is the surface hydrostatic stress; R is the gas constant; T is the temperature; F is the Faraday's constant and η is the overpotential. As it can be seen in this equation, an additional mechanical symmetry factor is introduced to account for the value of the hydrostatic stress. The mechanical symmetry factor is usually an adjustable parameter depending on the value of the hydrostatic stress. This is necessary, due to the excessive hydrostatic stress at the surface leading to very high values of the first exponential term in Eq. 2. This compensation by tuning the mechanical symmetry factor could be realized by introducing the hydrostatic stress to the exchange current density. Since, usually, the exchange current density 51 $(i_0 = Fkc^{1-\beta})$ is a function of concentration and the rate constant only, its value should be scaled to match the hydrostatic exponential term. In a full electro-mechanical model of a battery, the exchange current density should be depended on species concentration, temperature, and also the nature of the electrode-electrolyte interface. Each of these contributions can significantly change the

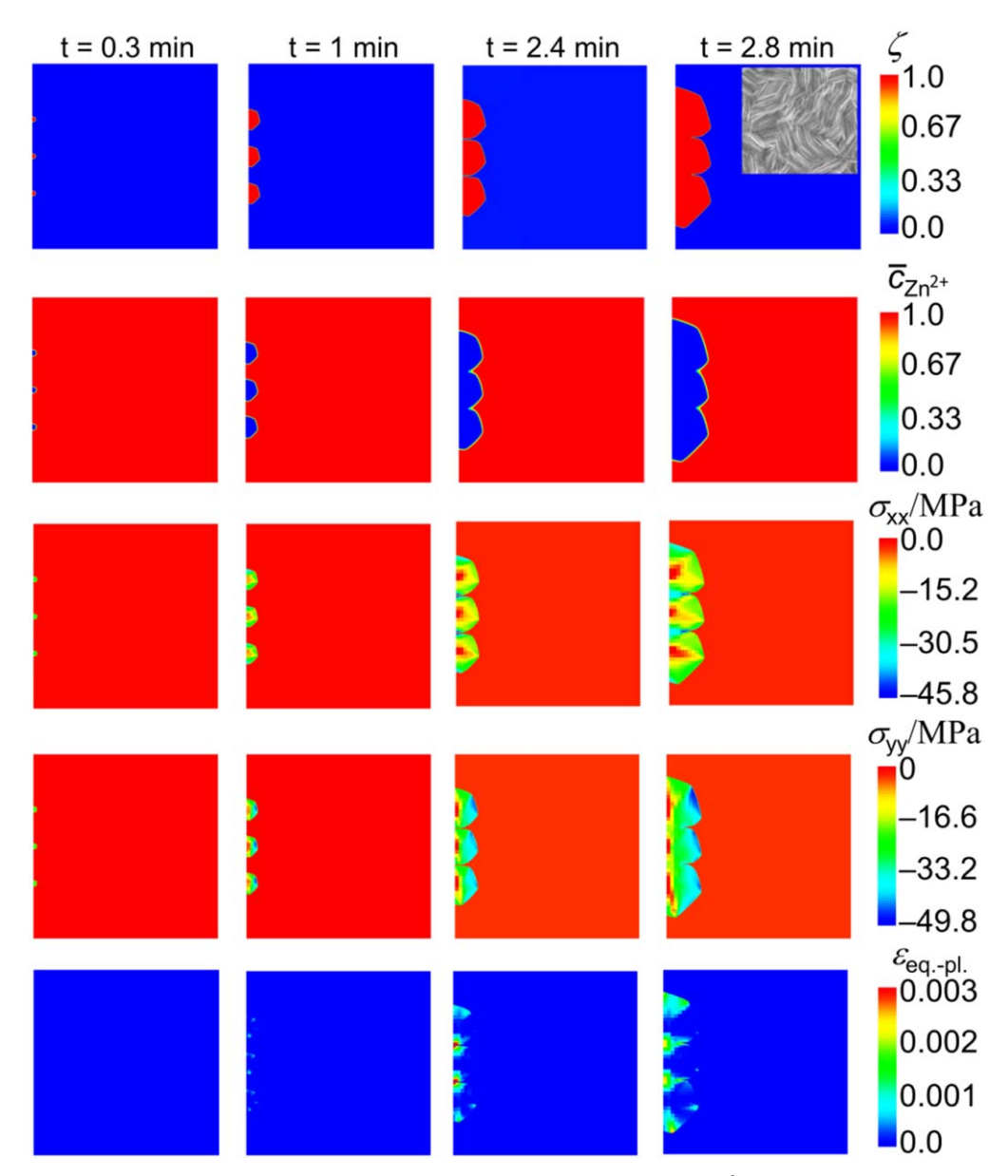


Figure 6. The PFM simulation results of the Zn electrodeposition at the current density of 15 mA·cm⁻². First row shows solid Zn boulders and filaments formation; second row depicts the change of Zn²⁺ concentration in the electrolyte; the third and fourth rows show the normal stress components (σ_{xx} and σ_{yy}); the fifths row demonstrates illustrates the equivalent plastic strain.

values of the exchange current density. In order to quantify the influence of the nature of the electrode-electrolyte interface, nanoscopic experiments should be performed to identify the structural and physico-chemical details of electrode subsurface layer. In a continuum model (mean-field approach) the unknown nature of electrode-electrolyte interface could be modeled by introducing a hydrostatic stress to the exchange current density as suggested above. During the Zn electrodeposition at the electrode-electrolyte interface both the electrode surface state and the SEI layer, which is in direct contact with the electrode surface, contribute to the interfacial stress development. Thus, the developed interfacial hydrostatic stress directly reflects the change of the nature of the electrode-electrolyte interface, as it is foreseen by the exchange current density.

Conclusions

The main objective of the present work is to understand Zn electrodeposits morphology in Zn aqueous battery at different current densities. Our results are mainly applicable to the aqueous

electrolyte with a near neutral pH, where surface layer ZnO is beneficial to electrodeposition. The approach is based primarily upon the prediction of different Zn morphologies reported in prior literature utilizing the PFM method and the analysis of the electrochemo-mechanical behavior during the deposition. The 2D model develops and applies an extended PFM to predict the Zn morphologies, the ions concentration, the electrostatic potential, the stress and the equivalent plastic strain. Materials' properties needed for the PFM calculations (e.g., Zn surface energy, Zn electric properties, etc.) are taken from the previously published data. Three regimes are investigated, specifically, low, intermediate and high current densities. For all current densities, the electrodeposition starts with the formation of hexagonal boulders following the crystal structure of Zn. However, depending upon the values of the current density, different morphologies are developed at the later stages. Specifically, at low current density the boulders transition to the filaments without interaction is observed, whereas at the intermediate current density both stress field as well as the SEI non-uniformity cause the formation of filaments and bushes. At the very high current density,

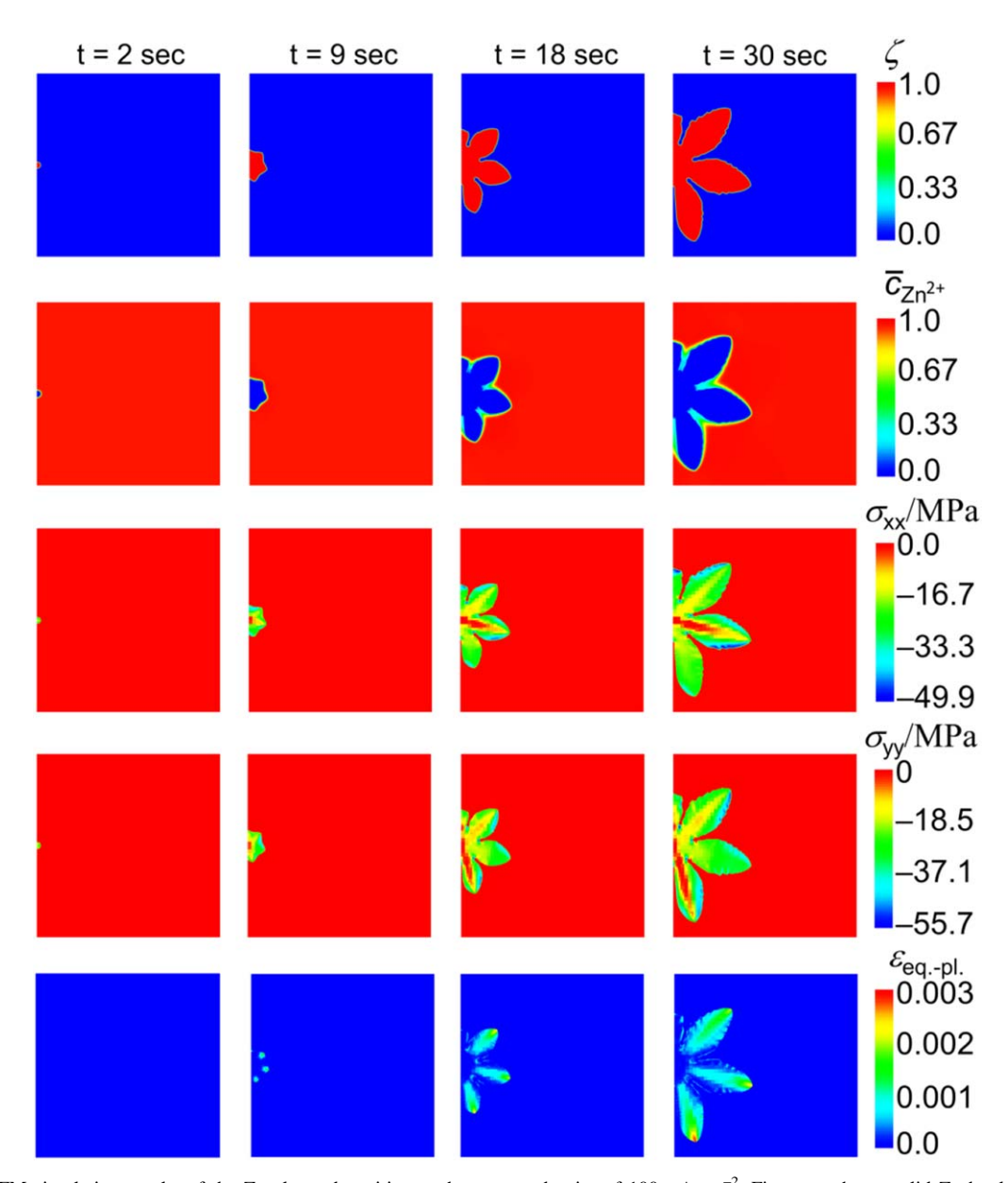


Figure 7. The PFM simulation results of the Zn electrodeposition at the current density of 100 mA·cm⁻². First row shows solid Zn boulders and filaments formation; second row depicts the change of Zn²⁺ concentration in the electrolyte; the third and fourth rows show the normal stress components (σ_{xx} and σ_{yy}); the fifths row demonstrates illustrates the equivalent plastic strain.

the formation of true dendritic morphology is observed causing the formation of sharp "leaves."

The 2D PFM developed in this work is clearly a simplification of the actual 3D electrode microstructure, where numerous in- and out- of-plain effects may influence the Zn electrodeposition. However, the relatively efficient computational cost allows a parametric study that can enable the fundamental understanding of rate-determining steps in Zn electrodeposition. Notwithstanding that the PFM provides the capabilities to deal with the real reconstructed electrode microstructures, modeling a specific electrode structure does not directly provide a predictive capability to suggest alternative protective strategies. Thus, modeling random structures as employed in the present work provides valuable insight and predictive capabilities. Therefore, based upon a new fundamental understanding gained in this work concerning the influence of current density on Zn electrodeposition morphologies, alternative protective strategies against Zn dendrites formation could be developed.

Acknowledgments

The authors acknowledge the financial support from the National Science Foundation award CBET-1805938. In addition, we would like to acknowledge the Advanced Cyberinfrastructure for Education and Research (ACER) group at The University of Illinois at Chicago (URL: https://acer.uic.edu). The MOOSE team and especially Dr. Daniel Schwen are gratefully acknowledged for helping in the development of the model and many insightful discussions on the topic presented in this work.

ORCID

Vitaliy Yurkiv https://orcid.org/0000-0002-3407-891X

References

- A. R. Mainar, E. Iruin, L. C. Colmenares, A. Kvasha, I. de Meatza, M. Bengoechea, O. Leonet, I. Boyano, Z. Zhang, and J. A. Blazquez, *J. Energy Storage*, 15, 304 (2018)
- M. I. Purcell, T. D. Hatchard, R. J. Sanderson, and M. N. Obrovac, *J. Electrochem. Soc.*, 161, A643 (2014).

- 3. T. Otani, M. Nagata, Y. Fukunaka, and T. Homma, Electrochim. Acta, 206, 366
- 4. D. Desai, D. E. Turney, B. Anantharaman, D. A. Steingart, and S. Banerjee, J. Phys. Chem. C, 118, 8656 (2014).
- 5. J. Huang, X. Chi, Q. Han, Y. Liu, Y. Du, J. Yang, and Y. Liu, J. Electrochem. Soc., 166, A1211 (2019).
- 6. T. Foroozan, V. Yurkiv, S. Sharifi-Asl, R. Rojaee, F. Mashayek, and R. Shahbazian-Yassar, ACS Appl. Mater. Interfaces, 11, 44077 (2019).
- 7. S. J. Banik and R. Akolkar, J. Electrochem. Soc., 160, D519 (2013).
- 8. T. Otani, Y. Fukunaka, and T. Homma, Electrochim. Acta, 242, 364 (2017).
- 9. J. F. Parker, C. N. Chervin, E. S. Nelson, D. R. Rolison, and J. W. Long, Energy Environ. Sci., 7, 1117 (2014).
- 10. D. Stock, S. Dongmo, K. Miyazaki, T. Abe, J. Janek, and D. Schröder, J. Power Sources, 395, 195 (2018).
- 11. Z. Yan, E. Wang, L. Jiang, and G. Sun, RSC Adv., 5, 83781 (2015).
- 12. M. Schmid and M. Willert-Porada, *Electrochim. Acta*, 260, 246 (2018).
- 13. T. Michlik, M. Schmid, A. Rosin, T. Gerdes, and R. Moos, *Batteries*, 4, 12 (2018).
- 14. C. Shen, X. Li, N. Li, K. Xie, J. Wang, X. Liu, and B. Wei, ACS Appl. Mater. Interfaces, 10, 25446 (2018).
- 15. T.-H. Wu, Y. Zhang, Z. D. Althouse, and N. Liu, Mater. Today Nano, 6, 100032 (2019)
- 16. A. Wang, S. Kadam, H. Li, S. Shi, and Y. Qi, NPJ Comput. Mater., 4, 15 (2018).
- 17. P. Barai, K. Higa, and V. Srinivasan, J. Electrochem. Soc., 164, A180 (2017).
- 18. S. Hu, Y. Li, K. M. Rosso, and M. L. Sushko, J. Phys. Chem. C, 117, 28 (2013).
- 19. V. Yurkiv, T. Foroozan, A. Ramasubramanian, R. Shahbazian-Yassar, and F. Mashayek, MRS Commun., 8, 1285 (2018).
- 20. D. A. Cogswell, Phys. Rev. E. Stat. Nonlin. Soft Matter Phys., 92, 011301 (2015).
- 21. V. Yurkiv, T. Foroozan, A. Ramasubramanian, R. Shahbazian-Yassar, and F. Mashayek, *Electrochim. Acta*, 265, 609 (2018).
- 22. L. Chen, H. W. Zhang, L. Y. Liang, Z. Liu, Y. Qi, P. Lu, J. Chene, and L.-Q. Chen, J. Power Sources, 300, 376 (2015).
- 23. Z. Hong and V. Viswanathan, ACS Energy Lett., 3, 1737 (2018).
- 24. X. Zeng, J. Hao, Z. Wang, J. Mao, and Z. Guo, Energy Storage Mater., 20, 410 (2019).
- 25. P. Bai, J. Li, F. R. Brushett, and M. Z. Bazant, *Energy Environ. Sci.*, 9, 3221 (2016).
- 26. A. Kushima, K. P. So, C. Su, P. Bai, N. Kuriyama, T. Maebashi, Y. Fujiwara, M. Z. Bazant, and J. Li, Nano Energy, 32, 271 (2017).
- 27. P. P. Trigueros, J. Claret, F. Mas, and F. Sagués, J. Electroanal. Chem., 312, 219 (1991).

- 28. J. Steiger, D. Kramer, and R. Mönig, Electrochim. Acta, 136, 529 (2014).
- 29. J. C. Bilello, D. Dew-Hughes, and A. T. Pucino, J. of Appl. Phys., 54, 1821 (1983).
- 30. Q. Zhao, M. J. Zachman, W. I. Al Sadat, J. Zheng, L. F. Kourkoutis, and L. Archer, Sci. Adv., 4, 1https://advances.sciencemag.org/content/4/11/eaau813110.1126/ sciady.aau8131 (2018).
- 31. L. Suo et al., J. Am. Chem. Soc., 139, 18670 (2017).
- 32. J. E. Guyer, W. J. Boettinger, J. A. Warren, and G. B. McFadden, Phys. Rev. E, 69, 021603 (2004).
- 33. J. E. Guyer, W. J. Boettinger, J. A. Warren, and G. B. McFadden, Phys. Rev. E, 69, 021604 (2004).
- 34. M. Z. Bazant, Acc. Chem. Res., 46, 1144 (2012).
- 35. M. R. Tonks, D. Gaston, P. C. Millett, D. Andrs, and P. Talbot, Comput. Mater. Sci., 51, 20 (2012).
- R. Kobayashi, Phys. D, 63, 410 (1993).
- 37. A. Ramasubramanian, V. Yurkiv, A. Najafi, A. Khounsary, R. Shahbazian-Yassar, and F. Mashayek, J. Electrochem. Soc., 164, A3418 (2017).
- A. F. Bower, Applied Mechanics of Solids (CRC Press, Taylor & Francis Group, Boca Raton, FL, USA) pp. 821 (2010).
- 39. D. R. Gaston, J. W. Peterson, C. J. Permann, D. Andrs, A. E. Slaughter, and J. M. Miller, *J. Open Res. Softw.*, **2**, 1 (2014).
- 40. V. Yurkiv, J. S. Gutierrez-Kolar, R. R. Unocic, A. Ramsubramanian, R. Shahbazian-Yassar, and F. Mashayek, J. Electrochem. Soc., 164, A2830 (2017).
- 41. D. A. Cogswell and M. Z. Bazant, ACS Nano, 6, 2215 (2012).
- 42. K. Raeissi, A. Saatchi, and M. A. Golozar, J. Appl. Electrochem., 33, 635 (2003).
- 43. H. M. Ledbetter, J. Phys. Chem. Ref. Data, 6, 1181 (1977).
- 44. J. G. Albright and D. G. Miller, J. Solution Chem., 4, 809 (1975)
- 45. A. Desalvo, P. Gondi, F. A. Levi, and F. Zignani, Nuovo Cim., XXXI, 904 (1964). 46. D. Desai, X. Wei, D. A. Steingart, and S. Banerjee, J. Power Sources, 256, 145
- (2014).
- 47. X. B. Cheng, R. Zhang, C.-Z. Zhao, F. Wei, J.-G. Zhang, and Q. Zhang, Adv. Sci., 3, 1https://www.ncbi.nlm.nih.gov/pmc/articles/PMC5063117/pdf/ADVS-3-1500213. pdf 1500213 (2015).
- 48. D. R. Ely and R. E. García, J. Electrochem. Soc., 160, 662 (2013).
- 49. N. Kotak, P. Barai, A. Verma, A. Mistry, and P. P. Mukherjee, J. Electrochem. Soc., 165, A1064 (2018).
- 50. B. Wu and W. Lu, J. Mech. Phys. Solids, 125, 89 (2019).
- 51. C. Monroe and J. Newman, J. Electrochem. Soc., 150, A1377 (2003).